Research Article Vol. 36, No. 11 / November 2019 / Journal of the Optical Society of America B 3181

Journal of the Optical Society of America B

OPTICAL PHYSICS

Design and analysis of a 0.9 Tb/s six-channel WDM filter based on photonic crystal waveguides

HARAPRASAD MONDAL, MRINAL SEN,* AND KAMANASHIS GOSWAMI

Department of Electronics Engineering Indian Institute of Technology (Indian School of Mines), Dhanbad, Jharkhand 826004, India
**Corresponding author: mrinal.sen.ahm@gmail.com*

Received 29 July 2019; revised 19 September 2019; accepted 30 September 2019; posted 2 October 2019 (Doc. ID 374077); published 28 October 2019

A six-channel wavelength-division multiplexing filter is proposed in this paper, based on a two-dimensional rods-in-air square-lattice photonic crystal (PhC) slab structure. The plane wave expansion method is applied to compute the band structure of the PhC. Three-dimensional finite-difference time-domain simulation methodology is used to measure and analyze the performance of the filter. Performances for both the 2D and 3D designs of the structure are analyzed. The analyses show that the device is capable of filtering six different wavelengths, i.e., 1310 nm, 1415 nm, 1455 nm, 1550 nm, 1725 nm, and 1770 nm. Owing to its linear optical operation, the device is able to operate at low power and also offers a high data rate in the range of ≈ 0.9 Tb/s to ≈ 4 Tb/s. Moreover, the footprint area of the proposed device is on the order of 165 μm^2, which is suitable for high-density integration of photonic circuits. © 2019 Optical Society of America

https://doi.org/10.1364/JOSAB.36.003181

1. INTRODUCTION

In this era, a world without digital computing and communication cannot be imagined. A massive amount of data exchange is taking place at every second everywhere on the globe, and the demand is growing continually. This growing demand is presently supported by an optical fiber communication system, which provides high-speed data transfer. However, speed of the system is constrained by optical–electronics–optical signal conversions at the data processing/switching nodes. A cluster of researchers, by virtue of the supreme speed of light, are motivated to replace these nodes by all-optical photonic integrated circuits (PICs) [1–3]. All optical PICs are made of optical waveguides utilizing phenomena such as self-phase modulation [4], cross-phase modulation [5], four-wave mixing [6], stimulated Raman scattering [7], light beam interference [8], self-collimation [9–11], plasmonic effect [12–14], etc. In this context, the photonic crystal (PhC) [15] waveguide has gained the most interest of researchers in designing all-optical devices/switches for PICs, as it inherits several beneficial phenomena of light guidance, such as bandgap guidance, self-collimation, temporal confinement (slow light), etc. PhC is a periodic arrangement of dielectric materials in one, two, or three dimensions, and the photonic bandgap (PBG) [16] is one of the key properties of a PhC. PBG shows transmittance/reflectance characteristics through/from the crystal for a range of frequencies. Defects are introduced by removing/modifying rods or holes on a PhC structure to control propagation of optical signal through the defect, bending, or other structural element of the PhC. A significant number of research works in two-dimensional PhC (2D-PhC) platforms, such as multiplexer and de-multiplexer [17–20]; power splitter [21,22]; adder [23–25]; subtractor [26]; polarizer [27]; decoder [28–30]; logic gates [31–35]; comparator [36], filter [37], etc., have been reported in the recent past. Among these, the optical wavelength filter is a crucial component, without which a wavelength-division multiplexing (WDM) communication system is paralyzed.

Sheng et al. [37] have proposed an all-optical four-channel wavelength demultiplexer based on a square lattice 2D-PhC made of rods-in-air structure. The 2D finite-difference time-domain (2D-FDTD) method has been used to evaluate its performance. However, its height is considered as infinite, which makes its out-of-plane loss for the complete spectrum to be null in contrast to practicality. Moreover, height of a practical/realistic PhC is always finite, for which its bandgap becomes narrower than that of its 2D evaluation, and hence, the structure proposed in [37] is not sufficient in practical scenarios. Similarly, Sinha and Rawal [38] reported a Y-shaped dual-band all-optical wavelength demultiplexer using rods-in-air as well as holes-in-slab 2D-PhC structures. The devices have been designed to filter only two optical wavelengths (1310 nm and 1550 nm), where the simulations have been performed in the 2D-FDTD method, and therefore, practical constraints limit their use, as stated above. On the other hand, Kannaiyan et al. [39] have shown the design and performance analysis of an eight-channel demultiplexer using rods-in-air 2D-PhC structure having eight quasi-square-ring resonators. In this work,

different quasi-square-ring resonators consisting of rods having different refractive indices (ranging from 3.16 to 3.86 in a step of 0.1) have been used. However, designing of a number of rods in a single PhC with such variations in refractive indices is quite challenging, and no particular material or process technology for the same has been mentioned in this work. Moreover, radii of some rods in this design have been considered with a variation of 1 nm, which makes it impractical to realize.

Therefore, in order to mitigate the above shortfalls, the work presented here first explores a composite optical material whose refractive index can be changed desirably based on the ratio of its constituents. This is discussed in the second section of the paper. Thereafter, the material is used to design a PhC-based six-channel optical filter to extract out the wavelengths of 1310 nm, 1415 nm, 1455 nm, 1550 nm, 1725 nm, and 1770 nm. Details of the device structure are presented in the third section, along with its band diagram and corresponding analysis. In the fourth section, a 2D-FDTD simulation technique is initially employed to evaluate the approximate characteristics of the device, where different performance metrics such as contrast ratio, data rate, and response time are calculated. Nevertheless, in order to assess the feasibility of operation of the device, the 3D model of the device is analyzed through a 3D-FDTD method in the fifth section. The simulations show that the ultra-compact device is able to exert a significant extinction ratio on all of its ports and, at the same time, deliver a high data rate. Finally, a conclusion on the whole work is drawn in the last section of the paper.

2. SELECTION OF MATERIAL FOR DESIGNING THE DEVICE

Design of the proposed device considers two different types of refractive indices (e.g., 3.4 and 3.6) for the rods of the PhC structure. However, it is quite challenging to design a single PhC with two different materials. On the other hand, the material property of a portion of the PhC can be changed by using ion implantation or selective diffusion. In view of that, the composite optical material aluminum gallium antimonide $Al_xGa_{1-x}Sb$ is considered for designing the device. The refractive index profile of the $Al_xGa_{1-x}Sb$ is highly dependent on the molar fraction x, and its dispersion can be estimated through the Sellmeier equation as follows [40]:

$$n^2 = A + B\frac{\lambda^2}{\lambda^2 - c^2}, \tag{1}$$

where n is the refractive index, λ is the operational wavelength expressed in nanometer, and the constants are

$$A(x) = 14.07 - 4.80x - 0.66x^2,$$
$$B(x) = 0.458 - 0.099x + 1.258x^2,$$
$$C(x) = 1486 - 2308x + 1973x^2.$$

The refractive index profile of the $Al_xGa_{1-x}Sb$ with respect to various values of x has been calculated at the wavelength of 1550 nm and is shown in Fig. 1(a). It can be observed in the figure that the refractive index of the $Al_xGa_{1-x}Sb$ can be engineered to 3.4 or 3.6 for a value of x as 0.8 or 0.4, respectively. Moreover, the dispersion relationships of the $Al_xGa_{1-x}Sb$ for $x = 0.4$ and 0.8, which are used to design the fundamental

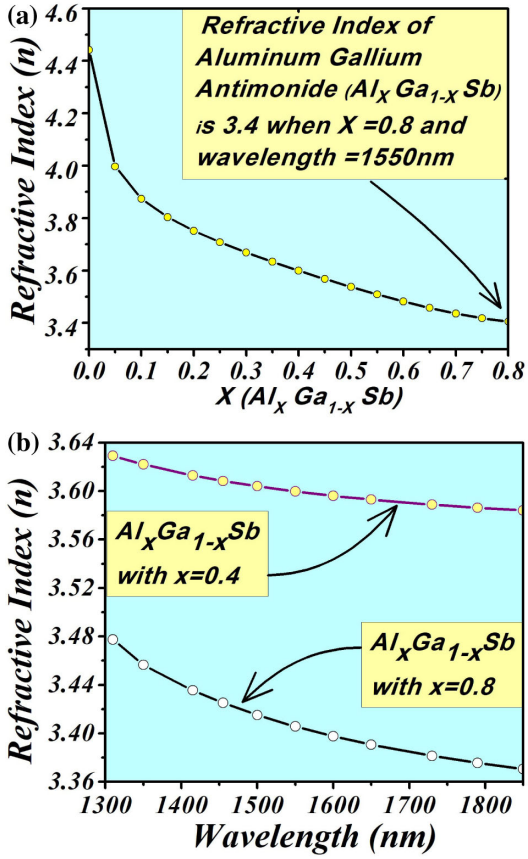

Fig. 1. Refractive index profile of $Al_xGa_{1-x}Sb$ (a) with various values of x when operational wavelength is 1550 nm and (b) with respect to wavelength when $x = 0.4$ and 0.8.

structure of the PhC, have also been calculated and are shown in Fig. 1(b). The curve for $Al_{0.4}Ga_{0.6}Sb$ shows that the deviation in refractive index is merely 3.6 ± 0.02 for the whole operating wavelength range (i.e., 1300 nm to 1800 nm) of the device.

3. MODEL DESCRIPTION AND PRINCIPLE OF OPERATION

Design of the proposed all-optical wavelength filter is shown in Fig. 2(a). The filter is made of a PhC, where $Al_{0.4}Ga_{0.6}Sb$-based pillars/rods (of refractive index 3.6) are considered to be arranged in a square lattice. Fabrication of such a structure may be realized following the similar process steps as described in [41–44]. Lattice constant (a) and diameter of the rods are taken as 580 nm and 197 nm, respectively. This is done in order to enable bandgap guidance of a large range of wavelengths through a W1 waveguide of the design and has been established by obtaining photonic band diagram of the PhC through a 2D plane wave expansion (PWE) method [45]. The complete dispersion diagram (i.e., for the wave-vector range gamma-X-M-gamma) for the transverse magnetic (TM) polarization modes is shown in Fig. 2(b), which shows that there is a large bandgap, i.e., the TM-polarized light in the range of frequencies within the bandgap would not be able to penetrate the structure in any direction. Thereafter, the projected band diagram for the W1 line defect PhC is calculated and shown in Fig. 3(a),

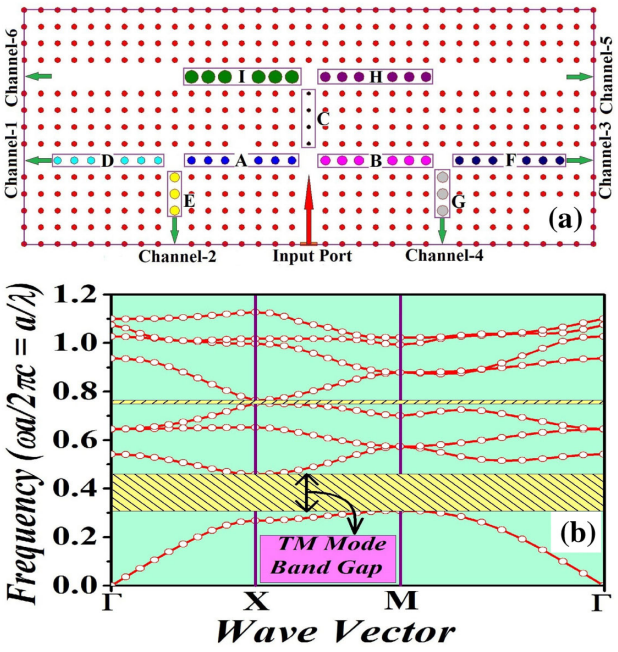

Fig. 2. Diagram of (a) proposed six-channel WDM filter and (b) complete photonic band diagram for background crystal.

which includes only the TM-guided modes [as transverse electric (TE)-polarized lights do not encounter bandgap guidance within the structure]. The figure shows that a W1 waveguide of the PhC supports bandgap-guided single-mode propagation for a TM-polarized light of normalized frequency ($f = a/\lambda$) ranging between 0.315 and 0.459 (corresponding to the wavelengths ranging from 1841 nm to 1263 nm).

Now, W1 line defects have been formed by removing rods in Γ-X direction of the PhC to construct waveguides and input/output ports. The proposed device has one input port, which coveys six different wavelengths, i.e., 1310 nm, 1415 nm, 1455 nm, 1550 nm, 1725 nm, and 1770 nm, to six different output ports, i.e., channel-1, channel-2, channel-3, channel-4, channel-5, and channel-6, respectively. Further line defects have been introduced within the waveguides to achieve this wavelength selective filtering operation. To create these line-defects, nine sets of dielectric rods of refractive index 3.4 (considered to be made of $Al_{0.8}Ga_{0.2}Sb$) have been introduced at different sections of the PhC. Among these sets, "A," "B," "D," "F," "H," and "I" contain six dielectric rods in each, "E" and "G" contain three dielectric rods in each, and set "C" contains four dielectric rods. Placements and diameters of these sets of rods are optimized to form a "tree" network of waveguides/channels where the "equi-level" nodes carry different ranges of wavelengths from each other. Also, the "children" nodes split up the wavelength range of the parent to a number of wavelength ranges. Here, sets A, B, and C are three equi-level waveguide nodes that split up the total wavelength range in three regions, i.e., 1240–1450 nm, 1380–1710 nm, and 1570–1880 nm, respectively. In order to obtain this target, diameters of the dielectric rods of sets A, B, and C are taken, respectively, as 276 nm, 334 nm, and 130 nm, based on their projected band diagrams, which are chronologically shown in Figs. 3(b)–3(d). Although these projected bands accommodate wider ranges of wavelengths than those specified above,

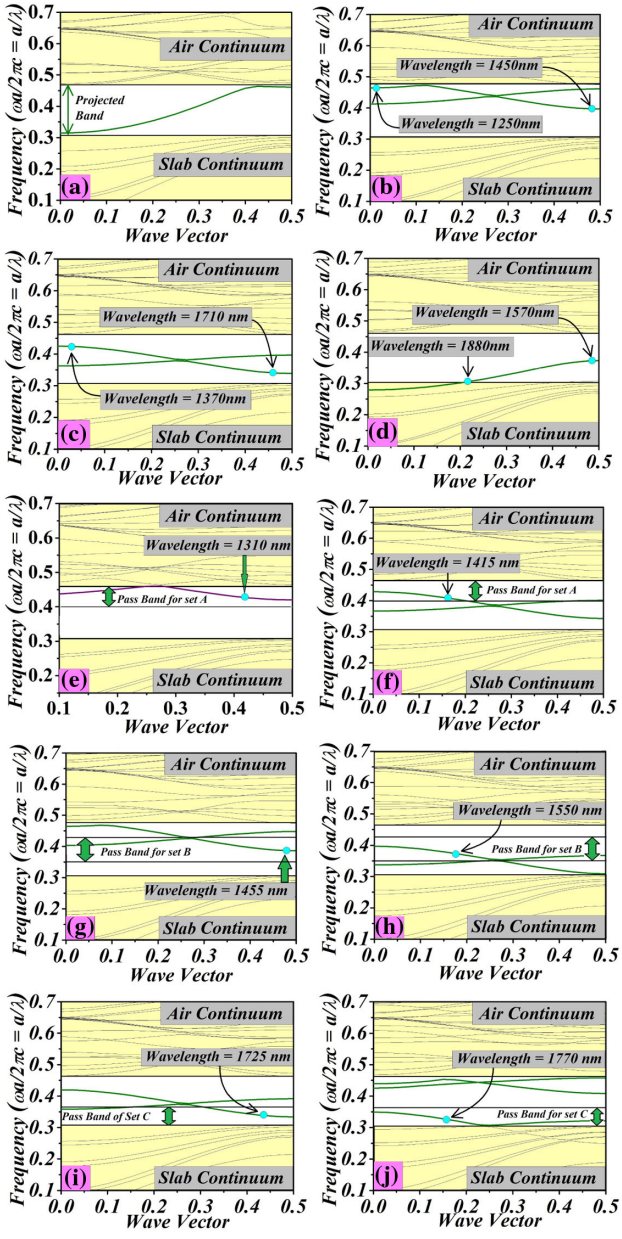

Fig. 3. Projected band diagram for (a) 2D PhC structure in TM mode, (b) defect rod "A," (c) defect rod "B," (d) defect rod "C," (e) defect rod "D," (f) defect rod "E," (g) defect rod "F," (h) defect rod "G," (i) defect rod "H," and (j) defect rods "I".

the wavelengths near their band edges experience high wave impedance. Thus, in spite of having some overlapping range of wavelengths in two adjacent waveguides, a wave follows the least impedance path and trails to a single direction. Thereafter, D and E, having diameters of 254 nm and 330 nm and being fed with the wavelength range 1240–1450 nm by the output of A, filter out the wavelengths 1310 nm and 1455 nm through output channels-1 and -2, respectively. This is supported by their band diagram, as shown in Figs. 3(e) and 3(f), respectively. On the other side, the output of set B directs the wavelengths in the range of 1380–1710 nm to its children nodes, i.e., set F and G, whose diameters are, correspondingly, 286 nm and 370 nm. However, their projected band diagrams, shown in Figs. 3(g)

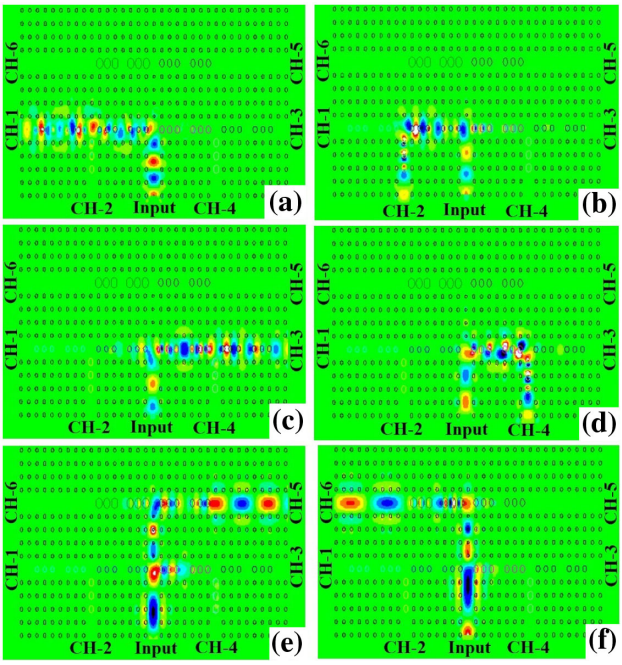

Fig. 4. 2D FDTD simulation results for (a) 1310 nm signal at channel-1, (b) 1415 nm signal at channel-2, (c) 1455 nm signal at channel-3, (d) 1550 nm signal at channel-4, (e) 1725 nm signal at channel-5, and (f) 1770 nm signal at channel-6.

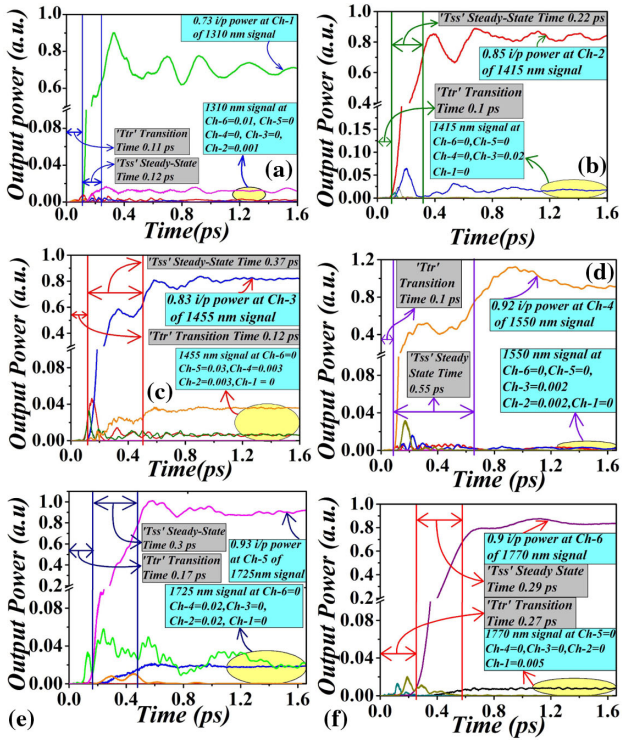

Fig. 5. Time-evolving and output power graph for (a) output channel-1, (b) output channel-2, (c) output channel-3, (d) output channel-4, (e) output channel-5, and (f) output channel-6.

and 3(h), respectively, allow the wavelength ranges of 1475–1850 nm and 1260–1500 nm. Hence, wavelengths 1455 nm and 1550 nm are filtered out from channel-3 (through set F) and channel-4 (through set G), respectively. Similarly, sets H and I are the children nodes of set C. Corresponding diameters of these sets are 340 nm and 430 nm, which allow propagation of the wavelengths 1725 nm and 1700 nm, respectively, to channels-5 and -6, as can be seen from their respective bands in Figs. 3(i) and 3(j). Thus, six different frequencies are collected from six different output channels of the filter.

Moreover, L1 micro-cavities have been introduced in the middle of A, B; A, D; B, F; and H, I, in order to increase output power levels at the corresponding ports. The whole design is made within a footprint of merely 164.84 μm^2.

4. RESULTS AND ANALYSES

A 2D-FDTD [46] algorithm has been applied to simulate the behavior of the proposed filter. Six different simulations have been performed by applying continuous-wave lights of wavelengths 1310 nm, 1415 nm, 1455 nm, 1550 nm, 1725 nm, and 1770 nm, however, one at a time. Electric field profiles for transmission of these wavelengths are shown in Figs. 4(a)–4(f), respectively. The figures depict that each different wavelength directs to a particular output channel, and their channel selectivity is remarkably good. Moreover, time-evolving normalized powers at each of the output channels for all the above wavelengths are obtained from these simulations, which are shown in Figs. 5(a)–5(f). These figures are further used in the following subsections to analyze performance of the optical filter against various metrics, such as transmission characteristics, extinction ratio, response time, and data rate.

A. Power Transmission Characteristics

Figures 5(a)–5(f) show the power transfer of every port for all the addressed wavelengths. It is noticed that 73% power of the applied input for the desired wavelength (i.e., 1310 nm) appears at channel-1. This loss in transmission is due primarily to the fact that the wavelength 1310 nm, which is to be filtered through channel-1, lies near a flat-band zone of the dispersion diagram of set A [Fig. 3(b)]. Moreover, the wavevector mismatch of the modes during propagation of the said wavelength from the input waveguide to set A and from set A to channel-1 is significantly large. These together increase the impedence, and hence attenuation, experienced by the wave. However, the percentage of power of the other wavelengths available at this channel is negligible. Similarly, the transmission losses of channels-2–6 are found about 0.7 dB, 0.8 dB, 0.36 dB, 0.31 dB, and 0.45 dB, respectively.

It may be noticed that a wave in a PhC waveguide usually experiences a significant scattering loss, which is on the order of 25 dB/cm for a group index as high as 20 [47]. However, this leads to a loss on the order of 0.05 dB in the proposed structure, where the maximum length of a waveguide is around 20 μm. Hence, this negligible loss has not been considered in the above calculation.

Table 1. Extinction Ratios for All Ports of the Optical Filter

Wavelength (λ)	Ch-1 (dB)	Ch-2 (dB)	Ch-3 (dB)	Ch-4 (dB)	Ch-5 (dB)	Ch-6 (dB)
1310 nm	—	28.63	48.63	48.63	48.63	18.63
1415 nm	59.29	—	16.28	59.29	59.29	59.29
1455 nm	59.19	24.41	—	24.41	27.66	59.19
1550 nm	59.63	38.21	26.62	—	59.63	59.63
1725 nm	59.19	17.42	59.19	15.21	—	59.19
1770 nm	22.3	59.29	59.29	59.29	59.29	—

Table 2. Steady-State Time, Bandwidth, and Bit Rate of Optical Filter

Signal (λ nm)	Output Port	Steady State Time (ps)	Bandwidth (THz)	Bit Rate (Tb/s) RZ 1 HZ = 0.5 (bits/s)	Bit Rate (Tb/s) NRZ 1 HZ = 1 (bits/s)
1310	Ch-1	0.12	4.1667	2.0833	4.1667
1415	Ch-2	0.22	2.2727	1.1364	2.2727
1455	Ch-3	0.37	1.3514	0.6757	1.3514
1550	Ch-4	0.55	0.9091	0.4545	0.9091
1725	Ch-5	0.30	1.6667	0.8333	1.6667
1770	Ch-6	0.29	1.7241	0.8621	1.7241

B. Extinction Ratio

The extinction ratio (ER) of an output channel can be defined as the ratio of powers of the desired signal to that of an undesired signal. Now, although every output channel has a single desired wavelength, all the other (undesired) wavelengths can also appear at the channel. Therefore, the number of ERs of a channel would be the same as that of the available input wavelengths (which can be restricted here to the available number of output ports). Therefore, each output channel in the proposed filter would have five different ERs for five undesired wavelengths, as calculated in Figs. 5(a)–5(f) and shown in Table 1. It is observed from the table that an ER over 48 dB is achieved at most of the channels for most of the undesired wavelengths. Conversely, the minimum ER is found as 15.21 dB at channel-4 for the wavelength 1725 nm, which is sufficiently good for rejecting a channel in WDM communication.

Here, it is worth mentioning that the ERs presented in Table 1 can be calculated from the S-parameters of the device. The S-parameters S12–S17 and S21–S71 are graphically shown in Figs. 9(a)–9(l), respectively, as functions of wavelengths.

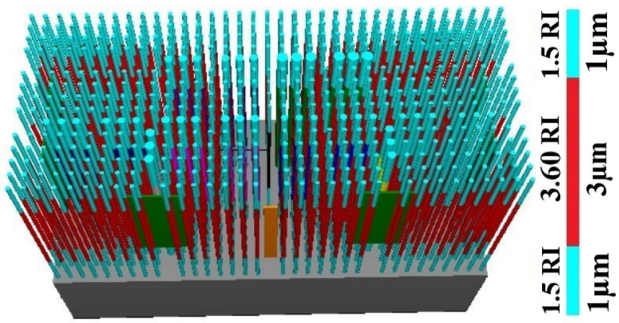

Fig. 6. 3D representation of six-channel all-optical wavelength filter.

C. Response Time and Data Rate

Response time and data rate: response time and data rate of the proposed filter have been measured from the time-evolving powers of different channels, as presented in Fig. 5. Response time [48] of a device is the sum of transition time (Ttr) and steady-state time (Tss). Ttr is defined as the time required for a signal to achieve 1% of its steady-state power at the desired output port. On the other hand, Tss is the time required for

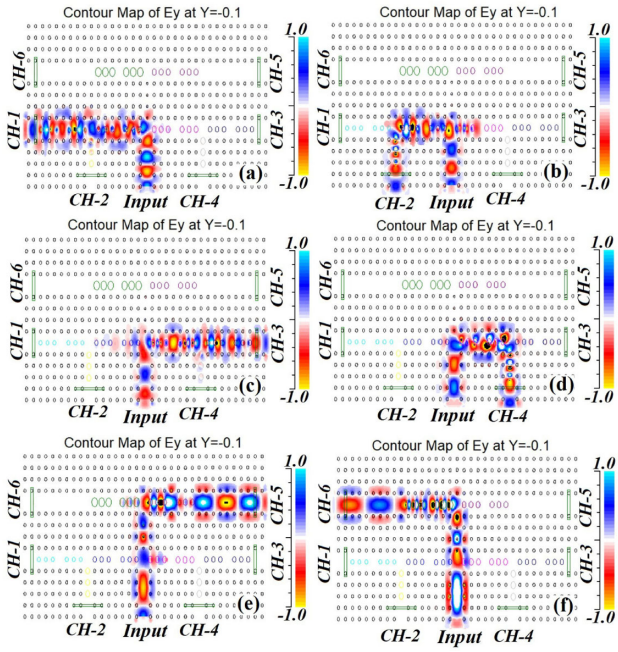

Fig. 7. 3D FDTD simulation of continuous wave for (a) 1310 nm wavelength at channel-1, (b) 1415 nm wavelength at channel-2, (c) 1455 nm wavelength at channel-3, (d) 1550 nm wavelength at channel-4, (e) 1725 nm wavelength at channel-5, and (f) 1770 nm wavelength at channel-6.

Table 3. Extinction Ratios for All Ports of the 3D Structure

Wavelength (λ)	Ch-1 (dB)	Ch-2 (dB)	Ch-3 (dB)	Ch-4 (dB)	Ch-5 (dB)	Ch-6 (dB)
1310 nm	—	12.05	22.72	20.85	31.63	21.46
1415 nm	13.01	—	14.62	14.52	22.52	16.90
1455 nm	21.55	18.77	—	13.27	22.05	20.88
1550 nm	15.22	14.84	12.87	—	16.68	16.90
1725 nm	22.34	16.02	30.47	15.68	—	16.90
1770 nm	31.66	17.27	20.65	19.29	21.36	—

a signal to reach from 1% to 90% of its steady-state output power. The Tss is quite important to calculate the bit rate at any output port. For example, the Tss at channel-1 (corresponding to the wavelength 1310 nm) is measured as ≈ 0.12 ps from its time-evolving graph, i.e., Fig. 5(a). Moreover, the falling time is also expected to be the same as the Tss, due to the linear optical operation of the device. Therefore, width of the narrowest pulse, which is the sum of rise time and fall time, becomes equal to 2xTss i.e., ≈ 0.24 ps. This leads to a bandwidth of the channel as 1/(2xTss), i.e., 4.1667 THz. Now, considering a return-to-zero (RZ) system, where the bit rate corresponds to half of the bandwidth, the bit rate of the system becomes 2.08 Tb/s. On the other hand, the same channel can offer a higher bit rate in a non-RZ (NRZ) system. Similarly, Tss, bandwidth, and bit rate for all the other output ports have also been calculated using the above-mentioned method from their time-evolving graphs, which are summarized in Table 2.

5. 3D CONSTRUCTION AND 3D-FDTD SIMULATION

A real device is supposed to be finite in all three directions, and hence, 3D analysis has been performed considering a slab height of ≈ 10 μm, which is shown in Fig. 6. The design considers that all the rods are 5 μm in height and have three layers along their lengths. While each of the top and bottom layers is 1 μm long, having a refractive index of 1.5, the 3 μm long middle layer has a refractive index of 3.6 or 3.4, depending on its characteristics (corresponding to non-defect rods or defect rods, respectively). This structure maintains the vertical symmetry of the PhC slab. Moreover, to achieve mechanical stability of the device, these rods are placed on a buffer oxide layer with a height of 5 μm (refractive index 1.5), which is sufficiently away from the evanescent field of the propagation modes. The footprint of the device is considered to be 174 μm^2 (20 μm × 8.7 μm).

A 3D-FDTD simulation method has been used to observe propagation profiles of the waves within the device. Propagation profiles for the waves of wavelengths 1310 nm, 1415 nm, 1455 nm, 155 nm, 1725 nm, and 1770 nm are chronologically shown in Figs. 7(a)–7(f). The simulation also enables us to calculate transmittance of different output channels (namely, channels-1–6) of the device, which are shown in Figs. 8(a)–8(f). It can be observed in Fig. 8 that the transmittance for the wavelengths 1.31 μm, 1.415 μm, and 1.455 μm at their respective output channels (i.e., channels-1, -2, and -3) are on the order of 0.6. This is, although a little less compared to their 2D simulation counterpart, sufficient for on-chip WDM filter

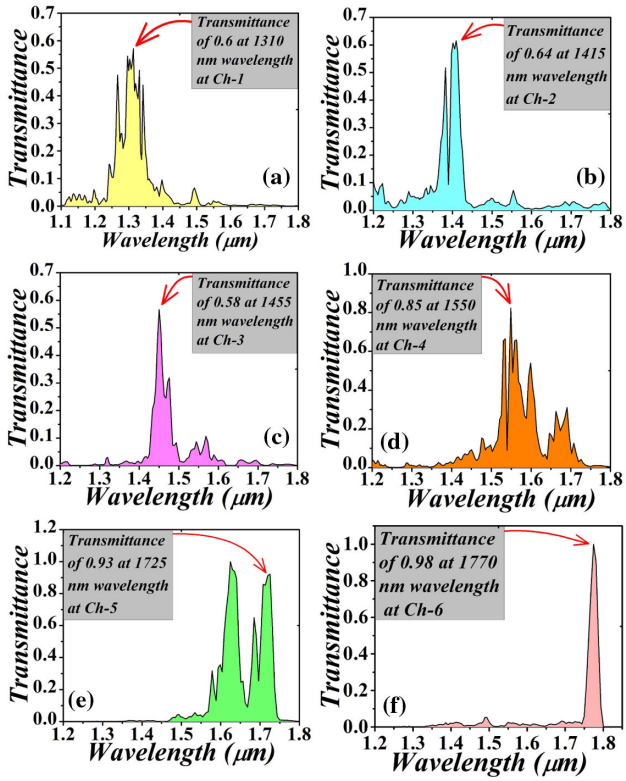

Fig. 8. Transmittance characteristics obtained in 3D structure for (a) output channel-1, (b) output channel-2, (c) output channel-3, (d) output channel-4, (e) output channel-5, and (f) output channel-6.

applications. On the other hand, channels-4, -5, and -6 (for the wavelengths 1.55 μm, 1.725 μm, and 1.77 μm) perform better and provide comparable transmittance (0.85, 0.93, and 0.98, respectively) as of the 2D-FDTD simulation. Moreover, the ER (or crosstalk) of every output channel obtained through this 3D-FDTD simulation is sufficiently close to those obtained by its 2D counterpart. The same for all the channels is tabulated in Table 3 for the convenience of the readers.

6. CONCLUSION

In this work, a six-channel WDM filter has been proposed based on PhC waveguides. The filter is capable of filtering the WDM wavelengths of 1310 nm, 1415 nm, 1455 nm, 1550 nm, 1725 nm, and 1770 nm. The design is made by considering a slab of $Al_xGa_{1-x}Sb$, having a refractive index of 3.6. The refractive index of some defect rods is considered as 3.4, which may

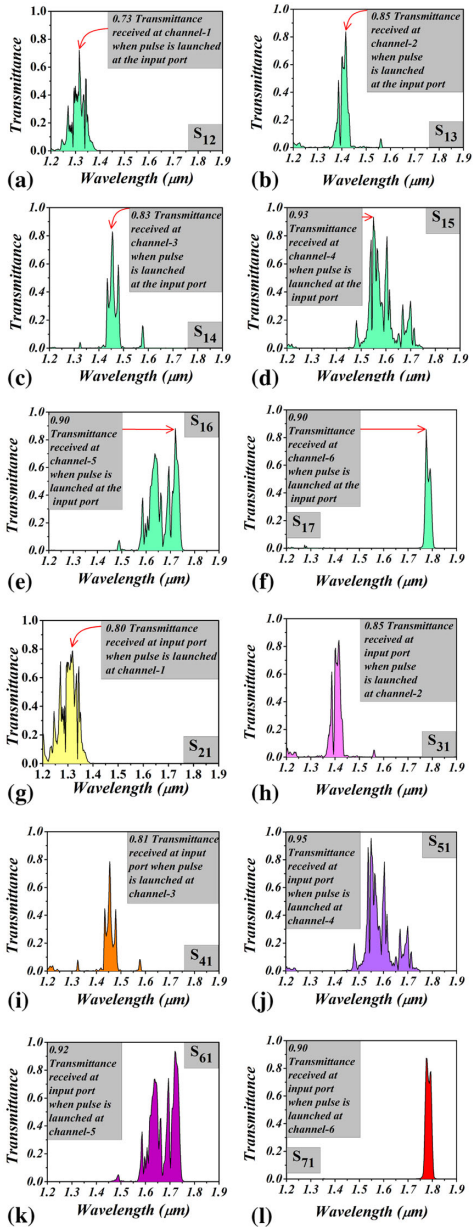

Fig. 9. S-Parameters: S12 and S13. (a) Power transfer characteristics from input (port-1) to channel-1 (port-2). (b) Power transfer characteristics from input (port-1) to channel-2 (port-3). S-Parameters: S14 and S15. (c) Power transfer characteristics from input (port-1) to channel-3 (port-4). (d) Power transfer characteristics from input (port-1) to channel-4 (port-5). S-Parameters: S16 and S17. (e) Power transfer characteristics from input (port-1) to channel-5 (port-6). (f) Power transfer characteristics from input (port-1) to channel-6 (port-7). S-Parameters: S21 and S31. (g) Power transfer characteristics from channel-1 (port-2) to input (port-1). (h) Power transfer characteristics from channel-2 (port-3) to input (port-1). S-Parameters: S41 and S51. (i) Power transfer characteristics from channel-3 (port-4) to input (port-1). (j) Power transfer characteristics from channel-4 (port-5) to input (port-1). S-Parameters: S61 and S71. (k) Power transfer characteristics from channel-5 (port-6) to input (port-1). (l) Power transfer characteristics from channel-6 (port-7) to input (port-1).

be achieved by changing the molar fraction (x) of the material. The band structure at different portions of the PhC has been calculated using the PWE method. Defect bands are molded by the choices of different radii of the sets of defect rods to enforce wavelength-selective filtering at different output channels. Performance of the device has been evaluated using a FDTD technique. A high ER on the order of ≈ 60 dB is achieved in most of the channels, along with a high data rate in the range of 0.5–2 Tb/s. Performance analysis of the 3D design of the device is also proved to be consistent with that of its 2D counterpart. Finally, the small footprint area of the device, on the order of 165 μm^2, makes the device suitable for its on-chip integration in PICs.

APPENDIX A

Figure 9 shows the different S-parameters of the 2D device. The input port is considered as port-1, and channel-1 to channel-6 are considered as port-2 to port-7, respectively.

REFERENCES

1. E. Yablonovitch, "Inhibited spontaneous emission in solid-state physics and electronics," Phys. Rev. Lett. **58**, 2059–2062 (1987).
2. M. A. Baqir, A. Farmani, T. Fatima, M. R. Raza, S. F. Shaukat, and A. Mir, "Nanoscale, tunable, and highly sensitive biosensor utilizing hyperbolic metamaterials in the near-infrared range," Appl. Opt. **57**, 9447–9454 (2018).
3. A. Alipore, A. Farmani, and A. Mir, "High sensitivityand tunable nanoscale sensor based on plasmon-induced transparency in plasmonic metasurface," IEEE Sens. J. **18**, 7047–7054 (2018).
4. W. J. Tomlinson, R. H. Stolen, and C. V. Shank, "Compression of optical pulses chirped by self-phase modulation in fibers," J. Opt. Soc. Am. B **1**, 139–149 (1984).
5. B. E. Olsson, P. Ohlen, L. Rau, and D. J. Blumenthal, "A simple and robust 40-Gb/s wavelength converter using fiber cross-phase modulation and optical filtering," IEEE Photon. Technol. Lett. **12**, 846–848 (2000).
6. K. Inoue, "Four-wave mixing in an optical fiber in the zero-dispersion wavelength region," J. Lightwave Technol. **10**, 1553–1561 (2012).
7. M. Sen and M. K. Das, "Raman mediated all-optical cascadable inverter using silicon-on-insulator waveguides," Opt. Lett. **38**, 5192–5195 (2013).
8. Y. Fu, X. Hu, and Q. Gong, "Silicon photonic crystal all-optical logic gates," Phys. Lett. A **377**, 329–333 (2013).
9. M. Noori, M. Soroosh, and H. Baghban, "Self-collimation in photonic crystals: application and opportunities," Ann. Phys. **530**, 1700049 (2017).
10. M. Noori and M. Soroosh, "A comprehansive comparison of photonic band gap and self-collimation based 2D square array waveguides," Optik **126**, 4775–4781 (2015).
11. M. Noori, M. Soroosh, and H. Baghban, "Highly efficient self-collimation based waveguide for mid-IR application," Photon. Nanostruct. Fundam. Appl. **19**, 1–11 (2016).
12. A. Farmani, A. Mir, and Z. Sharifpour, "Broadly tunable and bidirectional terahertz graphene plasmonic switch based on enhanced Goos-Hanchen effect," Appl. Surf. Sci. **453**, 358–364 (2018).
13. A. Farmani, A. Mir, M. Bazgir, and F. B. Zarrabir, "Highly sensitive nano scale plasmonic biosensor utilizing fano resonance metasurface in THz range: numerical study," Phys. E: Low dim. Sys. Nanostruct. **104**, 233–240 (2018).
14. A. Farmani, "Three dimensional FDTD analysis of a nanostructured plasmonic sensor in the near-infrared range," J. Opt. Soc. Am. B **36**, 401–407 (2019).
15. J. D. Joannopoulos, S. G. Johnson, J. N. Winn, and R. D. Meade, *Photonic Crystals: Molding the Flow of Light*, 2nd ed. (Princeton University, 2008).
16. J. H. Yuan and Y. Y. Lu, "Photonic bandgap calculations with Dirichletto-Neumann maps," J. Opt. Soc. Am. **23**, 3217–3222 (2006).
17. D. Gogoi, K. Das, H. Mondal, P. Talukdar, and K. Hussain, "Design of ultra-compact 3-channel wavelength demultiplexer based on photonic crystal," in *Proceedings of the International Conference*

on Automatic Control and Dynamic Optimization Techniques (ICACDOT), Pune, India (2016), pp. 590–593.
18. R. Talebzadeh, M. Soroosh, Y. S. Kavian, and F. Mehdizadeh, "Eight channel all-optical demultiplexer based on photonic crystal resonant cavities," Optik **140**, 331–337 (2017).
19. H. Mondal, K. Goswami, C. Prakash, and M. Sen, "An all-optical ultra-compact 4-channel wavelength de-multiplexer," in *Proceedings of the 3rd International Conference on Microwave and Photonics (ICMAP)*, Dhanbad, India (2018), pp. 1–2.
20. H. A. Banaei, F. Mehdizadeh, and S. Serajmohammadi, "A novel 4-channel demultiplexer based on photonic crystal ring resonators," Optik **124**, 5964–5967 (2013).
21. M. Noori, M. Soroosh, and H. Baghban, "Design of highly efficient polarization beam splitter based on self-collimation on Si platform," J. Mod. Opt. **64**, 491–499 (2017).
22. H. Saghaei, A. Zahedi, R. Karimzadeh, and F. Parandin, "Line defects on As2Se3 chalcogenide photonic crystals for the design of all optical power splitter and digital logic gates," Superlattices Microstruct. **110**, 133–138 (2017).
23. Q. Liu, Z. Quyang, C. Jung Wu, C. P. Liu, and J. C. Wang, "All-optical half adder based on cross structures in two-dimensional photonic crystals," Opt. Express **16**, 18992–19000 (2008).
24. M. M. Karkhanehchi, F. Parandin, and A. Zahedi, "Design of an all optical half-adder based on 2D photonic crystals," Photon. Netw. Commun. **33**, 159–165 (2017).
25. S. Serajmohammadi, H. A. Banaei, and F. Mehdizadeh, "Proposal for realizing an all-optical half adder based on photonic crystals," Appl. Opt. **57**, 1617–1621 (2018).
26. F. Parandin, M. R. Malmir, and M. Naseri, "All-optical half-subtractor with low-time delay based on two-dimensional photonic crystals," Superlattices Microstruct. **109**, 437–441 (2017).
27. C. Prakash, M. Sen, H. Mondal, and K. Goswami, "Design and optimization of a TE-pass polarization filter based on a slotted photonic crystal waveguide," J. Opt. Soc. Am. B **35**, 1791–1798 (2018).
28. F. Parandin, M. M. Karkhanehchi, M. Naseri, and A. Zahedi, "Design of a high bitrate optical decoder based on photonic crystal," J. Comput. Electron. **17**, 830–836 (2018).
29. H. Mondal, M. Sen, and K. Goswami, "Design and analysis of all-optical 1 to 2 line decoder based on linear photonic crystal," IET Optoelectron. **13**, 191–195 (2019).
30. F. Mehdizadeh, H. A. Baneai, and S. Serajmohammadi, "Design and simulation of all optical decoder based on nonlinear PhCRRs," Optik **156**, 701–706 (2018).
31. H. Mondal, S. Chanda, M. Sen, and T. Datta, "All optical AND gate based on silicon photonic crystal," in *Proceedings of the International Conference on Microwave and Photonics (ICMAP)*, Dhanbad, India (2015), pp. 1–2.
32. H. Mondal, S. Chanda, and P. Gogoi, "Realization of all-optical logic AND gate using dual ring resonator," in *Proceedings of the International Conference on Automatic Control and Dynamic Optimization Techniques (ICACDOT)*, Pune, India (2016), pp. 553–556.
33. E. H. Shaik and N. Rangaswami, "Design of photonic crystal- based all-optical AND gate using T-shaped waveguide," J. Mod. Opt. **63**, 941–949 (2016).
34. H. Mondal, M. Sen, C. Prakash, K. Goswami, and C. Sarma, "Impedance matching theory to design an all optical AND gate," IET Optoelectron. **12**, 244–248 (2018).
35. A. Farmani, A. Mir, and M. Irannejad, "2D-FDTD simulation of ultra-compact multifunctional logic gate with nonlinear photonic crystal," J. Opt. Soc. Am. B **36**, 811–818 (2019).
36. S. Serajmohammadi, H. A. Banaei, and F. Mehdizadeh, "A novel proposal for all optical 1-bit comparator using nonlinear PhCRRs," Photon. Nanostruct. Fundam. Appl. **34**, 19–23 (2019).
37. L. J. Sheng, L. Han, and Z. Lee, "Compact four-channel terahertz demultiplexer based on directional coupling photonic crystal," Opt. Commun. **350**, 248–251 (2015).
38. R. K. Sinha and S. Rawal, "Modeling and design of 2D photonic crystal based Y type dual band wavelength demultiplexer," Opt. Quantum Electron. **40**, 603–613 (2008).
39. V. Kannaiyan, R. Savarimuthu, and S. K. Dhamodharan, "Performance analysis of an eight channel demultiplexer using a 2D-photoniccrystal quasi square ring resonator," Opto-Electron. Rev. **25**, 74–79 (2017).
40. R. Ferrini, M. Patrini, and S. Franchi, "Optical functions from 0.02 to 6 eV of Al_x Ga_{1-x} Sb/GaSb epitaxial layers," J. Appl. Phys. **84**, 4517–4524 (1998).
41. P. Bienstman, S. Assefa, S. G. Johnson, J. D. Joannopoulos, G. S. Petrich, and L. A. Kolodziejski, "Taper structures for coupling into photonic crystal slab waveguides," J. Opt. Soc. Am. B **20**, 1817–1821 (2003).
42. S. Assefa, P. T. Rakich, P. Bienstman, S. G. Johnson, G. S. Petrich, J. D. Joannopoulos, L. A. Kolodziejski, E. P. Ippen, and H. I. Smith, "Guiding 1.5 micrometer light in photonic crystals based on dielectric rods," Appl. Phys. Lett. **85**, 6110–6112 (2004).
43. T. Shih, A. Kurs, M. Dahlem, G. Petrich, M. Soljacic, E. Ippen, L. Kolodziejski, K. Hall, and M. Kesler, "Supercollimation in photonic crystals composed of silicon rods," Appl. Phys. Lett. **93**, 131111 (2008).
44. A. A. M. Kok, C. M. Heesch, E. J. Geluk, M. J. H. Jochem, J. J. G. M. van der, Y. S. Oei, and M. K. Smit, "Two-dimensional photonic crystals based on In Prods," in *Proceedings of the IEEE/LEOS Benelux Chapter*, Eindhoven, The Netherlands (2006), pp. 273–276.
45. S. G. Johnson and J. D. Joannopoulos, "Block-iterative frequency domain methods for Maxwell's equations in a plane wave basis," Opt. Express **8**, 173–190 (2001).
46. W. Huang, S. Chu, and S. Chaudhuri, "A semi-vectorial finite difference time-domain method (optical guided structure simulation," IEEE Photon. Technol. Lett. **3**, 803–806 (1991).
47. L. O'Faolain, S. A. Schulz, D. M. Beggs, T. P. White, M. Spasenovic, L. Kuipers, F. Morichetti, A. Melloni, S. Mazoyer, J. P. Hugonin, P. Lalanne, and T. F. Krauss, "Loss engineered slow light waveguides," Opt. Express **18**, 27627–27638 (2010).
48. P. Rani, Y. Kalra, and R. K. Sinha, "Design and analysis of polarization independent all-optical logic gates in silicon-on-insulator photonic crystal," Opt. Commun. **374**, 148–155 (2016).